Published in final edited form as:
Opt Express. 2009 March 2; 17(5): 3861–3877.

In Vivo Functional Imaging of Intrinsic Scattering Changes in the Human Retina with High-speed Ultrahigh Resolution OCT

V. J. Srinivasan[1], **Y. Chen**[1,2], **J. S. Duker**[2], and **J. G. Fujimoto**[1,*]

[1]Department of Electrical Engineering and Computer Science and Research Laboratory of Electronics, Massachusetts Institute of Technology, Cambridge, Massachusetts 02139

[2]New England Eye Center, Tufts Medical Center, Boston, Massachusetts 02116

Abstract

Non-invasive methods of probing retinal function are of interest for the early detection of retinal disease. While retinal function is traditionally directly measured with the electroretinogram (ERG), recently functional optical imaging of the retina has been demonstrated. In this manuscript, stimulus-induced, intrinsic optical scattering changes in the human retina are measured *in vivo* with high-speed, ultrahigh resolution optical coherence tomography (OCT) operating at 50,000 axial scans per second and ~3.3 micron axial resolution. A stimulus and measurement protocol that enables measurement of functional OCT retinal signals is described. OCT signal changes in the photoreceptors are demonstrated. Two distinct responses having different temporal and spatial properties are reported. These results are discussed in the context of optical intrinsic signals measured previously in the retina by fundus imaging and scanning laser ophthalmoscopy. Finally, challenges associated with *in vivo* functional retinal imaging in human subjects are discussed.

1. Introduction

Functional impairment may precede clinically significant structural changes in many retinal diseases. There are several objective methods for measuring the functional response of the retina and optic nerve including multifocal electroretinography (ERG) [1,2], pattern ERG [3, 4], visual evoked potentials [5,6], multifocal visual evoked potentials [7-13], and pupil perimetry [14-16]. Optical imaging of intrinsic retinal signals may provide additional information about function that cannot be obtained by electrical recordings alone. Optical imaging techniques have been previously applied in the brain to measure small changes in optical properties caused by membrane depolarization and cell swelling in the cortex [17,18].

Optical intrinsic signal imaging in the retina measures stimulus-induced changes in the optical properties of retinal tissues. Typically, a visible light stimulus is used to activate the retina and near-infrared observation light is used to monitor retinal reflectance. Near-infrared observation light minimizes pre-stimulation of the retina, and avoids the effects of absorption changes caused by photopigment bleaching. Fundus CCD imaging studies in macaque monkey retinas using near-infrared observation light suggested that intrinsic signals result from a combination of inner retinal, outer retinal, and hemodynamic responses [19-22]. Fundus imaging of intrinsic signals has been performed in other animal models [23] and extended to human subjects [24,

*Corresponding author: jgfuji@mit.edu.

OCIS codes: (170.4500) Optical coherence tomography; (170.3880) Medical and biological imaging; (330.4300) Noninvasive assessment of the visual system; (330.5310) Photoreceptors; (330.5380) Physiology.

25]. While fundus imaging enables rapid assessment of a wide field, unambiguous assignment of response components to specific retinal layers was not possible. Fast light scattering changes in the amphibian retina have been measured using a number of optical imaging modalities including bright field, dark field, and cross-polarization microscopy [26,27], as well as OCT [28]. Recently, intrinsic signals from human cone photoreceptors were measured with a flood illumination adaptive optics camera [29]. Cone scintillation was measured using a self-interference effect which is especially sensitive to the refractive index of the outer segments. A related experiment was also performed with an adaptive optics scanning laser ophthalmoscope [30], which showed a clear increase in infrared light scattering in the stimulated region with respect to its surroundings in five out of fifteen subjects. There are numerous discrepancies in the properties of the functional signals measured by the studies mentioned above. This may be attributed to differences in experimental protocol, technology, and animal model, as well as a relatively complex retinal response which involves changes in multiple retinal layers.

Ultrahigh resolution time-domain OCT was previously used to observe local reflectivity changes in isolated rabbit retinas in response to a light stimulus [31]. The high axial resolution of OCT, enabled by coherence gating, allows localization of functional responses to individual retinal layers. Spectral / Fourier domain OCT [32,33] was applied to measure similar signals from the photoreceptors in anesthetized rats [34]. The high imaging speed of spectral / Fourier domain OCT enables three-dimensional raster scan protocols, which enable correlation and speckle averaging to correct for motion during functional experiments.

In order to apply functional optical imaging of the retina clinically, measurements must be performed in awake human subjects. One limitation of spectral / Fourier domain OCT systems is that sensitivity depends on axial position or imaging depth [35,36]. Therefore, axial motion artifacts may cause undesirable fluctuations in measured signal. In animal experiments, this problem can be mitigated by immobilization of the animal. In unanaesthetized human subjects, fluctuations in axial eye position as small as tens of microns can cause noise on the order of a few percent, which may obscure small intrinsic signals. Additionally, a non-intrinsic change caused by accommodation, fixation changes, or axial motion artifacts which is repeatable across multiple trials may lead to a statistically significant result. Therefore, statistical significance alone is not sufficient to demonstrate an intrinsic response and careful experimental design and choice of controls is required.

In this study, an *in vivo* method of measuring localized, intrinsic scattering changes with OCT in the human retina is presented. Multiple responses from the photoreceptor layer are demonstrated with differing signs and time courses.

2. Experimental methods

2.1 System description

The OCT system schematic is shown in Fig. 1(a). The experimental setup used a tungsten halogen lamp coupled to a multimode fiber which was imaged onto the retina to form a 380 micron spot. The stimulus position was changed using a galvanometer. The scanning OCT beam and the stimulus were combined using a dichroic mirror before the scan lens of the ophthalmic scanning unit. Therefore, both the stimulus and the OCT beam used the same scan lens and the same ocular lens. The retinal illuminance was 5×10^4 Td.

Ultrahigh resolution spectral/Fourier domain OCT systems can have a 10 dB sensitivity drop over 1 mm imaging depth in tissue, caused by the limited spectral resolution of high-speed spectrometers. Therefore, the measured interference signal from a layer in the retina with a constant backreflectance will vary due to involuntary eye motion, which changes the axial

position of the retina during imaging. This noise can mask intrinsic tissue reflectance changes due to functional activation. In functional OCT, it is crucial to minimize sources of noise that cause spurious reflectance changes.

To reduce the axial sensitivity drop, an alternative spectrometer design was used, shown in Fig. 1(b). A dual-grating spectrometer design was used to increase the spectral resolution and therefore increase the axial imaging range. Two 1200 lpmm gratings were used. The imaging lens was 80 mm focal length and the fiber collimating objective was 35 mm focal length. The angle of incidence at the second grating deviates from the Littrow condition at the edges of the spectrum, resulting in reduced diffraction efficiency. However, for this experiment the severity of the sensitivity drop was more important than the absolute sensitivity. Similar or better performance could have been achieved using longer focal length lenses and a single grating, however aberrations in longer focal length lenses and current availability of high efficiency, high line density holographic gratings imposed experimental limits. The light source was a Broadlighter D890 (Superlum, Ltd.), with a wavelength span from 800 nm to 1020 nm. The full-width at half maximum (FWHM) of the spectrum was approximately 150 nm. The Broadlighter was chosen over the Ti:Sapphire laser used in previous work [37] because of its higher spectral stability over time. In addition, the longer wavelength Broadlighter reduces possible pre-stimulation of the retina by the scanning OCT beam. The spectrometer used a 2048 pixel camera (Aviiva M4, e2V) with 10 bit A/D resolution, 4 taps, a 120 MHz total read rate, and a 14 micron pixel size. The imaging speed was 50,000 axial scans per second. The sensitivity was approximately 92 dB with 750 microwatts of incident power on the eye. The relatively low sensitivity was attributed to the lower efficiency of the dual-grating spectrometer and the high axial scan rate. The sensitivity versus imaging depth is shown in Fig. 1(c). The sensitivity drop is approximately linear on a dB scale over the first 1 mm in air. The axial resolution versus imaging depth is shown in Fig. 1(d). Resolution was measured as the full-width at half maximum (FWHM) of the point spread function amplitude. The measured axial resolution varied between 4.4 and 4.6 microns in air depending on axial delay (Fig. 1(d)). Assuming a tissue group refractive index of 1.36 and neglecting effects of water absorption, this corresponds to an axial resolution in tissue of around 3.3 microns. A theoretical axial resolution of 2.6 microns in tissue was obtained by numerical Fourier transformation of the Broadlighter spectrum. The measured axial resolution was significantly worse than the theoretical value due to shaping of the spectrum by the interferometer and spectrometer, and a slight truncation of the spectrum at the edges of the CCD line scan array.

2.2 Protocol 1 and data analysis

One normal, 26 year old male subject was imaged using protocol 1. The subject had stable fixation, and the head was stabilized using a chin rest and forehead rest. The retina was dark-adapted for 40 minutes prior to the experiment, but cycloplegics were not used. Multiple trials were performed during a single experiment, with 2 minutes between trials. An OCT raster scan was repeated, generating a series of 3D OCT data sets over time. A fundus photograph and OCT raster scan are shown in Fig. 2(a). The 3D OCT data set generated by this raster scan is unwrapped and flattened to the IS / OS junction, as shown in Fig. 2(b). Fig. 2(c) shows an *en face* image of the summed retinal signal, and Fig. 2(d) shows an *en face* image of the summed photoreceptor signal. Fig. 2(e) shows a single cross-sectional image from the 3D OCT data set with the outer retinal layers labeled. Fig. 2(f) shows a cross-sectional image from a 3D OCT data set acquired in the parafoveal region (not shown).

A pre-stimulus was applied near the fovea approximately 2 s prior to the actual measurement in order to avoid the severe initial eye motion artifacts during the actual measurement. The measured region for the first experiments (Fig. 4 - Fig. 6) was 4 degrees nasal to fovea. External fixation was used for the contralateral eye. *En face* frames consisted of 128 images × 168 axial

scans × 1024 axial pixels over a ~700 micron square (500 ms per frame, 2 frames per second). The stimulus was turned on at 0.5 s, after the baseline frame was acquired. A total of 3 frames were acquired after the stimulus was turned on. Each frame was assigned to a time point corresponding to the acquisition of the central position of that frame. Therefore, the 4 frames corresponded to time points t=0.25 s, t=0.75 s, t=1.25 s, and t=1.75 s. For a given trial, a random region of the field was illuminated, corresponding to either case 1 shown in Fig. 3(a) or case 2 shown in Fig. 3(b). Thus trials were assigned to one of two groups, depending on the illuminated region. The parameters, $\Gamma_1(t)$ and $\Gamma_2(t)$, which measure normalized amplitude reflectances from each region, were computed as follows.

$$\Gamma_1(t) = \left[r_{Sig}(t) / r_{Ref}(t) \right]_{Region1} \quad (1)$$

$$\Gamma_2(t) = \left[r_{Sig}(t) / r_{Ref}(t) \right]_{Region2} \quad (2)$$

The fractional changes in $\Gamma_1(t)$ and $\Gamma_2(t)$ were computed for both regions as shown below.

$$\Delta\gamma_1(t) = \frac{\Gamma_1(t) - \Gamma_{1,baseline}}{\Gamma_{1,baseline}} \quad (3)$$

$$\Delta\gamma_2(t) = \frac{\Gamma_2(t) - \Gamma_{2,baseline}}{\Gamma_{2,baseline}} \quad (4)$$

The subscripts 1 and 2 denote regions 1 and 2, as shown in Fig. 3(c). In Eq. (1) and Eq. (2), $r_{Sig}(t)$ is the amplitude reflectance from a layer which is expected to exhibit intrinsic scattering changes. $r_{Ref}(t)$ is the amplitude reflectance from a layer which is assumed not to exhibit intrinsic scattering changes. The amplitude reflectance r is related to the intensity reflectance R by $r=R^{1/2}$. In order to compute amplitude reflectances, $r_{Sig}(t)$ and $r_{Ref}(t)$, the anterior boundary of the photoreceptor inner segment / outer segment (IS / OS) junction was first detected in each 3D OCT data set. The segmentation algorithm was similar to that reported previously [38]. However, because the measured reflectances are highly sensitive to segmentation error, the capability for manually-aided boundary correction was added. To rule out experimental bias, the process of manual correction was performed based only on the OCT image and segmentation lines, without knowledge of the experimental parameters, and the illumination location was randomized. All axial positions were measured relative to the IS / OS junction anterior boundary, which served as a reference. To measure the amplitude reflectance from a given layer, a range of axial (Z) positions corresponding to that layer was first selected. The range of axial positions corresponding to a given layer (IS / OS, ROST, and RPE) was the same for all trials within an experiment for a given subject and retinal location. The median value of the OCT linear magnitude data was first computed for each axial scan over this range of axial (Z) positions. This yielded a median reflectance value for each axial scan. For each 3D OCT data set, this quantity was averaged over a set of transverse (x and y) positions. Division or normalization of reflectances was performed after transverse averaging. To determine appropriate areas for transverse averaging, each 3D OCT data set was cross-correlated with the baseline 3D OCT data set using the photoreceptor *en face* summation image (Fig. 2(d)). Cross-correlation determined overlapping portions of regions 1 and 2, as shown in

Fig. 3(c). Trials with excessive transverse eye motion of more than 150 microns relative to the baseline frame, or blinking which precluded segmentation were excluded from the analysis.

Finally, the difference between the fractional changes was computed as a function of time. The difference operation essentially compares the fractional change in normalized reflectance in region 1 ($\Delta\gamma_1(t)$) to the fractional change in normalized reflectance in region 2 ($\Delta\gamma_2(t)$).

$$\begin{aligned}\Delta\gamma(t) &= \Delta\gamma_1(t) - \Delta\gamma_2(t) \\ &= \Gamma_1(t)/\Gamma_{1,\text{baseline}} - \Gamma_2(t)/\Gamma_{2,\text{baseline}}\end{aligned} \tag{5}$$

Since there were four frames, $\Delta\gamma$ could be computed at four different time points: t = 0.25 s, t = 0.75 s, t = 1.25 s, and t = 1.75 s. Note that $\Delta\gamma(t=0.25s)=0$. The estimated local response, or the estimated local change in normalized reflectance in the illuminated region relative to the change in normalized reflectance in the non-illuminated region was plotted along with $\Delta\gamma(t)$ for each of the two groups. The post-stimulus average could also be computed by averaging over all times after the stimulus onset as follows.

$$\Delta\gamma_{\text{avg}} = \sum_{t>0.5s} \Delta\gamma(t) \tag{6}$$

The values of $\Delta\gamma_{\text{avg}}$ were compared between groups 1 and 2 using the Student's t-test. The imaging protocol and data analysis presented here uses reference layer normalization and comparison of two adjacent regions to account for possible motion artifacts. However, one disadvantage is that due to the comparison of adjacent regions of the retina in Eq. (5), only localized changes can be measured. Since this study emphasizes measurement of the photoreceptors, where intrinsic changes are expected to be co-localized with the illumination, the imaging protocol and data analysis are appropriate. However, to measure inner retinal neural or hemodynamic changes which may not be as well localized, other approaches may be required. Finally, the IS / OS junction reference boundary is useful in order to measure the outer retina, where the layers closely follow the contour of the IS / OS junction. In the inner retina, where the nerve fiber layer thickness and retinal contour change with eccentricity, the retinal layers do not follow the contour of the outer retina. Therefore, measurements of the inner retina are expected to show higher noise than outer retinal measurements.

2.3 Protocol2 and data analysis

Once spatial localization of the response was established using protocol 1, the scanning protocol was modified to reduce the size of a single 3D OCT data set by a factor of 3, thereby improving the temporal resolution by a factor of 3. Two normal male subjects (27 years old and 34 years old) were imaged using protocol 2. The subjects had stable fixation, and the head was stabilized using a chin rest and forehead rest. The time for dark-adaptation, time between trials, and pre-stimulus were identical to the above description for protocol 1. However, for protocol 2 *en face* frames consisted of 64 images × 112 axial scans × 1024 axial pixels (167 ms per frame, 6 frames per second). The modified protocol (protocol 2) is shown in Fig. 3(d)-3(f). The stimulus was turned on after the first frame, and off after the fourth frame. Due to the short stimulus duration, individual frames after the stimulus which showed more than 150 microns of motion were excluded without excluding the whole trial. The purpose of this protocol was to improve the temporal resolution and determine a return to baseline. The data analysis procedure was very similar to that described above for protocol 1, and is shown in Fig. 3(d)-3(f). Similarly, $\Delta\gamma_{\text{avg}}$ could be computed using selected time points after the stimulus, as shown in Eq. (7). Fig. 7 shows results obtained with this modified scanning protocol.

$$\Delta\gamma_{avg} = \sum_{t_1 \le t \le t_2} \Delta\gamma(t) \tag{7}$$

2.4 T-statistic

The t-statistic was used to compare values of $\Delta\gamma_{avg}$ between the two groups. The t-statistic is defined as:

$$t = \frac{m_1 - m_2}{\sqrt{\frac{s_1^2}{N_1} + \frac{s_2^2}{N_2}}} \tag{8}$$

In the above expression, m_1 and m_2 are the sample means, s_1 and s_2 are the sample standard deviations, and N_1 and N_2 are the sample sizes. The indices 1 and 2 refer to the two groups, determined by which side of the field of view is randomly selected for illumination (Fig. 3(a)-(b) and Fig. 3(d)-(e)).

In order to perform an unpaired t-test, the two samples must be random and independent and the sample mean difference, m_1-m_2, must be normally distributed. The t-test makes a hypothesis about the underlying population (the null hypothesis is that the two population means are equal), and calculates the distribution of the t-statistic under this hypothesis. A t-statistic is then computed based on the actual data. Based on the value of the t-statistic obtained from the actual data, the distribution can be used to calculate the probability of obtaining this value under the null hypothesis. If the population means are the same, then t in Eq. (8) has a t-distribution with zero mean and a shape determined by the number of degrees of freedom. It is possible to assign a probability or p-value to any particular value of t.

2.5 Sources of experimental noise and error

Possible sources of error in this series of experiments include pre-stimulation of the retina by the near-infrared light, axial motion, accommodation changes, and transverse motion. Transverse motion can be further classified as either motion within a frame or motion between frames. The random stimulus protocol, correlation with the baseline frame, and subsequent comparison between regions 1 and 2, shown in the above equations, were designed to mitigate all of the above errors, with the exception of transverse motion within a frame.

The normalization to a reference layer, shown in Eq. (1) and Eq. (2), helped to reduce signal changes caused by axial motion and severe accommodation changes. As shown in Fig. 1(c), the sensitivity drop is approximately linear on a dB scale over the first 1 mm in air, implying that the functional dependence is exponential with distance over this range. Therefore, the fractional change in signal caused by axial motion alone should be approximately the same for all retinal layers, and normalization should remove most of the variation caused by the axial sensitivity drop.

Comparison of fractional changes in two anatomically similar regions of the retina was performed in Eq. (5). The comparison of two portions of the retina illuminated equally by the near-infrared OCT light negates possible effects of pre-stimulation by the OCT light, which was previously mentioned as a confounding factor in functional OCT experiments [31]. Additionally, the random illumination protocol and comparison of adjacent spatial regions in the retina helps to distinguish between a spatially non-specific signal change, which could be a motion artifact, and a response co-localized with the illumination, which is more likely to be an intrinsic functional change.

To account for transverse motion artifacts between frames, each individual frame was correlated with the baseline frame to determine overlapping portions of region 1 and region 2, which were used to determine $\Gamma_{1,baseline}$, $\Gamma_{2,baseline}$, $\Gamma_1(t)$ and $\Gamma_2(t)$. Therefore, changes relative to baseline, shown in Eq. (3) and Eq. (4), were always computed using normalized amplitude reflectances obtained from the same transverse location. Transverse motion within a frame was not accounted for. In addition, the effects of stimulus position changes due to transverse motion were neglected.

3. Results

The results of the functional imaging experiment are presented in Fig. 4 - Fig. 7. Fig. 4 shows the IS / OS junction response ($r_{Sig}=r_{ISOS}$, $r_{Ref}=r_{RPE}$). Fig. 4(a) shows the individual trials, with $\Delta\gamma(t)$ plotted as a function of time. Fig. 4(b) shows the average time courses for each group in Fig. 3(a)-3(b). These results clearly show that the stimulus results in an increase in the normalized reflectance of the illuminated region relative to the non-illuminated region. Fig. 4 (c) shows a scatter plot of $\Delta\gamma_{avg}$, indicating the trial number along the horizontal axis. The difference between the two groups is statistically significant ($p < 1e\text{-}7$, two-tailed t-test).

While the procedure of reference layer normalization followed by comparison of adjacent regions yields statistically significant results, this procedure is complex. Fig. 5 shows the effect of individual steps in the procedure on the measured functional response. A qualitative comparison of $\Delta\gamma_{avg}$ scatter plots without (Fig. 5(a) and Fig. 5(c)) and with reference layer normalization (Fig. 5(b) and Fig. 5(d)) shows that reference layer normalization reduces the noise variance. A comparison of scatter plots without (Fig. 5(a) and Fig. 5(c)) and with comparison of adjacent regions (Fig. 5(e)) shows that comparison of adjacent regions also reduces the noise variance. Fig. 5(f) shows that reference layer normalization *and* comparison of adjacent regions results in the lowest overall noise variance.

In order to explore the spatial behavior of the functional response, the t-statistic was plotted as a function of axial position (Z) in Fig. 6(a)-6(b). The t-statistic plot is preferred over a plot of the average fractional change, which may be misleading since different retinal layers have different noise variances. Fig. 6(a) shows one unwrapped 3D OCT data set displayed as a two-dimensional image, with axial position (Z) along the horizontal axis. The 3D OCT data set was flattened to the IS / OSjunction and unwrapped prior to display and therefore does not show any axial variation in the IS / OS junction position. Therefore, Fig. 6 shows less detail than the images in Fig. 2(e)-2(f). The data set has been flattened to the IS / OS junction anterior surface, which occurs at a value of Z=250 microns. Fig. 6(b) shows the t-statistic as a function of axial position. For this analysis, r_{Sig} in Eq. (1) and Eq. (2) was the median reflectance from a 3 pixel window centered at axial position Z and averaged over the transverse plane. If r_{Sig} is allowed to vary as a function of Z, $\Delta\gamma_{avg}$ in Eq. (6) varies as a function of z as well. Therefore, the t-statistic, given in Eq. (8) can be computed at each axial position, as shown in Fig. 6(b). Two different values for the reference reflectance were used. For the red, dashed curve, the reference reflectance is the RPE reflectance, as in Fig. 4 ($r_{Ref}=r_{RPE}$). For the blue, dotted curve, the reference reflectance is the total retinal reflectance ($r_{Ref}=r_{Tot}$).

Fig. 6(b) shows a reflectance change which appears to be localized to the photoreceptor IS / OS junction. Both choices for normalization show that a positive peak in the t-statistic is seen at the position of the IS / OS junction. Logically, it makes sense to use a reference layer in which is close to the layer that is thought to exhibit intrinsic scattering changes. If this is the case, then the reference layer should help to normalize out signal variations due to the axial sensitivity drop as well as possible accommodation changes. Therefore, the t-statistic calculated using the RPE reflectance is higher and more sharply peaked than the t-statistic plot using the total retinal reflectance as the reference. Fig. 6(b) does not necessarily imply that

retinal layers other than the IS / OS junction do not exhibit intrinsic changes. Rather, Fig. 6(b) merely shows that for this particular choice of experimental parameters and normalization layers, any intrinsic changes in other layers were not found to be statistically significant.

The preceding results suggest that the photoreceptor layer functional response shows good correspondence with the illumination location. This suggests that spatial mapping of the fractional response may be possible. Fig. 6(c)-(6d) shows spatial maps of the differential response for the photoreceptor layer. Here, the differential response is calculated at each transverse (x,y) position for each trial.

$$m(x,y)=\frac{\left[\frac{r_{ISOS}(x,y)}{r_{RPE}(x,y)}\right]_{post-stimulus}-\left[\frac{r_{ISOS}(x,y)}{r_{RPE}(x,y)}\right]_{pre-stimulus}}{\left[\frac{r_{ISOS}(x,y)}{r_{RPE}(x,y)}\right]_{pre-stimulus}} \quad (9)$$

A spatial map is created for each trial. The spatial maps are then compounded over multiple trials by median filtering. Median filtering in the transverse (*en face)* plane is used to reduce noise from speckle as well as registration errors. As shown, the photoreceptor layer reflectance increase corresponds reasonably well with the illumination location, suggesting a localized response, since the differential increases seen in Fig. 6(c)-6(d) correspond well with the illumination patterns in Fig. 3(a)-3(b). Because of good correspondence between the illumination location and the functional response, a combined differential map can be formed by averaging all trials by flipping the differential maps from case 2 so that the illuminated regions correspond, as shown in Fig. 6(e). This is justified because the scanned region is relatively small and the photoreceptor morphology does not vary too much across this region.

Fig. 7 shows a comparison of the topographic t-statistic plots and time courses for the perifovea (7 degrees eccentricity) and periphery (13 degrees eccentricity), demonstrating two distinct response components. For this figure, protocol 2 shown in Fig. 3(d)-3(f) was used, and the number of axial scans per 3D OCT data set was reduced by a factor of 3 in order to increase the temporal resolution by a factor of 3. Fig. 7(a) shows the unwrapped 3D OCT data set from the perifovea along with the t-statistic ($0.58\ s \leq t \leq 0.92\ s$) plotted as a function of axial position. As expected based on the previous result, a clear peak is seen at the IS / OS junction. Fig. 7(b) shows a response similar to the response seen in Fig. 4(b), but with better temporal resolution. The response appears to return to baseline by t = 2.5 seconds. Individual trials are also shown in Fig. 7(c). Fig. 7(d) shows the t-statistic plot computed using later time points ($2.75\ s \leq t \leq 3.08\ s$). This plot shows a negative response from the rod outer segment tip (ROST) region, just anterior to the RPE. Fig. 7(d) does not show the positive IS / OS response seen in Fig. 7 (a) because the t-statistic is computed at a later time interval. Thenegative response means that the ROST layer reflectance decreases in the illuminated region relative to the non-illuminated region. Fig. 7(e) shows the average time course of this response, and Fig. 7(f) shows individual trials. Fig. 7(g) shows the unwrapped 3D OCT data set from the periphery along with the t-statistic as a function of axial position. The t-statistic plot does not show a positive peak at the IS / OS junction in the periphery. Instead, a negative peak in the t-statistic plot is seen in the region just anterior to the RPE, corresponding to the ROST region. The location scanned for Fig. 7(g) corresponds roughly to the same eccentricity as Fig. 2(e), which shows a rod-dominated morphology. Fig. 7(h) shows the average response at the ROST layer. The negative ROST response in the periphery shows a slower time course than the positive IS / OS response. The ROST response in the periphery continues to grow in magnitude even to t=3 seconds, while the IS / OS response appears to return to baseline after the stimulus is turned off. Fig. 7 (i) shows individual trials.

Both the IS / OS junction response and the ROST response were found to have similar magnitudes and time courses across subjects. Each of the responses was also reproduced with statistical significance in one subject across three experiments of approximately 20 trials each. The IS / OS junction response and the ROST response were present in the perifovea, but the IS / OS response was not detected at larger eccentricities. The ROST response was also found to be present in both the temporal and nasal peripheral retina. This suggests that intrinsic signals from the photoreceptors depend only on distance from the fovea (eccentricity), and further increases confidence that the observed changes are not due to motion artifacts.

Experiments were also performed under light-adapted conditions. The IS / OS junction response was found to be absent in one subject and negative in the other subject. Due to this ambiguity, the light-adapted response is not discussed in detail here.

4. Discussion

Intrinsic signal imaging is a well-established technique in the brain that measures structural or metabolic changes in living tissue. In the retina, preliminary studies have been performed using fundus imaging, suggesting a combination of neural and hemodynamic components that contribute to scattering changes. This paper demonstrates *in vivo* intrinsic signal imaging of photoreceptor changes in awake human subjects using ultrahigh resolution OCT.

4.1 Interpretation of layers

The interpretation of outer retinal morphology visualized on conventional ultrahigh resolution OCT retinal images has been discussed previously [38-40]. Fig. 2(e)-2(f) shows cross-sectional images extracted from 3D OCT data sets used for functional experiments. The outer retinal layers are labeled in the periphery (Fig. 2(e)) and parafovea (Fig. 2(f)) according to our interpretation. At the posterior boundary of the outer nuclear layer is the external limiting membrane (ELM). Posterior to the ELM, a reflective band represents the inner segment / outer segment (IS / OS) junction of the photoreceptors. Posterior to the IS / OS junction band are the cone outer segment tips (COST) [41]. Posterior to the COST is an additional band of high reflectance (ROST) that corresponds to the rod outer segment tips and the apical RPE processes that interdigitate with the rod outer segments. This band appears to be absent in the fovea. At the distal end of the retina are the retinal pigment epithelium (RPE) and Bruch's membrane (BM).

4.2 Interpretation of functional response and comparison with previous work

The positive signal from IS / OS junction reported here is probably associated with cone activity. Under light adapted conditions, the positive IS / OS response was absent and in some cases reversed sign. In addition, the IS / OS junction response was not detected in the periphery (Fig. 7(g)) where the cone density is considerably lower. The IS / OS junction response agrees with an adaptive optics scanning laser ophthalmoscope study by Grieve et al. [30], which reported positive changes in cone mosaic reflectance in five out of fifteen subjects. Interestingly, the same study reported that one of the measured subjects showed a decrease in cone mosaic reflectance. Based on our results, this apparent anomaly may be due to either insufficient dark-adaptation, or may be related to the negative ROST response which is discussed below. Additionally, the IS / OS junction response reported here may also be related to the cone scintillation effect [29]. Assuming that a change in the effective refractive index of the outer segment accounts for cone scintillation as well as the IS / OS reflectance changes reported here, the rise time of the IS / OS reflectance change should correspond roughly to the duration of scintillation (300−400 milliseconds). Although the IS / OS signals measured here (Fig. 4(b), Fig. 7(b)) appear to show a slightly longer rise time, this may be due to differences in stimulus retinal illuminance and duration. Finally, it is also important to note that the known

directionality of the IS / OS junction reflection implies that the observed intrinsic signals may also depend on the location and size of entrance and exit pupils during imaging. Future work is required to fully characterize this effect.

A negative response from the thin reflective band anterior to the RPE and posterior to the COST (cone outer segment tips) was also observed in the perifovea and periphery. This band was labeled ROST (rod outer segment tips) because it corresponds to the approximate location of the rod outer segments that interdigitate with the apical retinal pigment epithelial processes. The ROST band is not clearly visible in the fovea and parafovea since the cone outer segments are long and the highly reflective COST band extends closer to the RPE. As shown in Fig. 7 (e) and Fig. 7(h), the ROST response has a relatively slow time course, and is negative. It is interesting to note that both the negative sign and slow time course of the response agrees with previous fundus imaging studies in macaque monkeys[19, 20]. However, because of limited instrument resolution and the close anatomical relationship between the ROST layer and the RPE apical processes that interdigitate with the rod outer segments, the exact anatomical source of the ROST response is uncertain. Photomechanical changes in the photoreceptors or the RPE or changes in the interphotoreceptor matrix after phototransduction may also account for the changes attributed to the ROST layer. The precise etiology of this signal remains unknown, as the origin could either be the rod outer segments or the RPE.

The imaging and analysis protocol presented here was designed to detect intrinsic changes that are co-localized with the illumination. Both the ROST signal and the IS / OS signal were localized to the region of illumination. Normalization to the RPE layer was helpful in reducing noise; however, it was not necessary in order to observe the intrinsic signals. RPE reflectance may change in response to a light stimulus; furthermore the increase (decrease) of scattering from a layer proximal to the RPE would decrease (increase) signal from the RPE due to an increase (decrease) in the attenuation coefficient. If this were the case, normalization to the RPE layer would cause intrinsic signal changes to be overestimated. To show that the result does not depend on which layer is chosen as the reference, we have presented results with normalization to the RPE reflectance, normalization to the total retinal reflectance, and no normalization at all. While we cannot rule out possible stimulus-induced changes in RPE reflectance, if such changes exist they are below the detection limits imposed by experimental noise. Comparison of the randomly illuminated region to a nearby, non-illuminated region demonstrated that intrinsic signals were co-localized with the illumination, and further increased confidence that the reflectance changes are intrinsic. However, due to high noise levels, multiple trials were required in order to establish adequate confidence intervals for the fractional reflectance changes.

6. Conclusion

Previous intrinsic optical imaging studies in the primate retina have shown conflicting results in terms of the sign and duration of reflectance changes. It has been hypothesized that these discrepancies can be attributed to multiple retinal layers contributing to the measured response. However, the axial sectioning achieved by confocal and full-field imaging modalities is generally not sufficient to resolve individual anatomical layers in the retina. Using the axial resolution enabled by OCT, this study demonstrates multiple intrinsic signals originating from different axial locations: the photoreceptor IS / OS junction and the rod outer segment tip (ROST) region, just proximal to the RPE. The differing signs of the responses may help to account for discrepancies in previous studies, in which signals were integrated over multiple layers. The IS / OS junction signal, which is positive under dark-adapted conditions and observed in the cone-dominated regions of the retina, may be related to reflectance increases measured in previous adaptive optics studies [30]. The ROST response, which is negative and

observed in the periphery, may be related to the negative reflectance changes observed in fundus imaging studies [19,20].

Eye motion represents a significant challenge which must be addressed in order to achieve more reliable measurements of retinal intrinsic signals and eventually perform clinical studies. This may be accomplished by faster imaging speeds, active eye tracking, or improved post-processing methods. Experiments for this study were extremely time-consuming and cumbersome, as a single time point in a single trial required processing and segmentation of an entire 3D OCT data set. Overall, more than 200 trials and over 3000 3D OCT data sets were required to obtain and verify results presented here. Similar experiments in anesthetized non-human primate models would likely be less cumbersome due to lower physiological noise levels, would contribute further to understanding intrinsic signals, and would give more credibility to the results presented here. However, the results presented here show that optical measurements of retinal intrinsic signals are possible using OCT in awake, human subjects. The highest signal-to-noise measurements were obtained a few hundred milliseconds after the stimulus, before motion artifacts became very severe but after intrinsic changes occurred, as well as a few seconds after the stimulus, when the subject was able to re-fixate.

In conclusion, high-speed ultrahigh resolution OCT may be a useful tool to measure and interpret functional scattering changes in the retina. While intrinsic changes in the photoreceptors are interesting from a scientific perspective, the measurement of inner retinal neural or hemodynamic intrinsic signals would probably have more direct clinical utility, since they could be used to assess neural transduction and neurovascular coupling. These measurements would require even further improvements in technology or measurement protocols in order to enable the reduction of motion artifacts and the detection of extremely weak signals.

Acknowledgments

We would like to acknowledge scientific contributions and helpful advice from Iwona Gorczynska, Laurel Vuong, Jonathan Liu, and Ben Potsaid. This research was sponsored in part by the National Institutes of Health R01-EY11289-24, R01-EY13178-07, P30-20 EY008098; National Science Foundation BES-0522845; Air Force Office of Scientific Research, FA9550-07-1-0014 and Medical Free Electron Laser Program contract FA9550-07-1-0101; Massachusetts Lions Eye Research Fund; and Research to Prevent Blindness Unrestricted Grant.

References and links

1. Kondo M, Miyake Y, Horiguchi M, Suzuki S, Tanikawa A. Clinical evaluation of multifocal electroretinogram. Invest. Opthamol. Visual Sci 1995;36:2146–2150.
2. Vaegan, Sanderson G. Absence of ganglion cell subcomponents in multifocal luminance electroretinograms. Aust N Z J Ophthalmol 1997;25(Suppl 1):S87–90. [PubMed: 9267637]
3. Berninger TA, Arden GB. The pattern electroretinogram. Eye 1988;2(Suppl):S257–283. [PubMed: 3076152]
4. Mierdel P, Zenker HJ, Marre E. The pattern ERG in glaucoma: effect of pattern reversal time. Int. Opthamol 1992;16:211–214.
5. Greenstein VC, Seliger S, Zemon V, Ritch R. Visual evoked potential assessment of the effects of glaucoma on visual subsystems. Vision Res 1998;38:1901–1911. [PubMed: 9797966]
6. Watts MT, Good PA, O'Neill EC. The flash stimulated VEP in the diagnosis of glaucoma. Eye 1989;3:732–737. [PubMed: 2630354]
7. Baseler HA, Sutter EE, Klein SA, Carney T. The topography of visual evoked response properties across the visual field. Electroencephalogr. Clin. Neurophysiol 1994;90:65–81. [PubMed: 7509275]
8. Hood DC, Zhang X. Multifocal ERG and VEP responses and visual fields: comparing disease-related changes. Doc. Ophthalmol 2000;100:115–137.

9. Klistorner AI, Graham SL. Early magnocellular loss in glaucoma demonstrated using the pseudorandomly stimulated flash visual evoked potential. J. Glaucoma 1999;8:140–148. [PubMed: 10209732]
10. Klistorner AI, Graham SL, Grigg JR, Billson FA. Multifocal topographic visual evoked potential: improving objective detection of local visual field defects. Invest. Opthamol. Visual Sci 1998;39:937–950.
11. Graham SL, Klistorner A. The diagnostic significance of the multifocal pattern visual evoked potential in glaucoma. Curr. Opin. Ophthalmol 1999;10:140–146. [PubMed: 10537765]
12. Hood DC, Zhang X, Greenstein VC, Kangovi S, Odel JG, Liebmann JM, Ritch R. An interocular comparison of the multifocal VEP: a possible technique for detecting local damage to the optic nerve. Invest. Opthamol. Visual Sci 2000;41:1580–1587.
13. Graham SL, Klistorner AI, Grigg JR, Billson FA. Objective VEP perimetry in glaucoma: asymmetry analysis to identify early deficits. J. Glaucoma 2000;9:10–19. [PubMed: 10708226]
14. Kardon RH, Kirkali PA, Thompson HS. Automated pupil perimetry. Pupil field mapping in patients and normal subjects. Ophthalmology 1991;98:485–495. discussion 495−486. [PubMed: 2052302]
15. Kardon RH. Pupil perimetry. Curr. Opin. Ophthalmol 1992;3:565–570. [PubMed: 10147922]
16. Hong S, Narkiewicz J, Kardon RH. Comparison of pupil perimetry and visual perimetry in normal eyes: decibel sensitivity and variability. Invest. Opthamol. Visual Sci 2001;42:957–965.
17. Grinvald A, Frostig RD, Lieke E, Hildesheim R. Optical Imaging of Neuronal-Activity. Physiol Rev 1988;68:1285–1366. [PubMed: 3054949]
18. Villringer A, Chance B. Non-invasive optical spectroscopy and imaging of human brain function. Trends Neurosci 1997;20:435–442. [PubMed: 9347608]
19. Tsunoda K, Oguchi Y, Hanazono G, Tanifuji M. Mapping cone- and rod-induced retinal responsiveness in macaque retina by optical imaging. Invest. Opthamol. Visual Sci 2004;45:3820–3826.
20. Hanazono G, Tsunoda K, Shinoda K, Tsubota K, Miyake Y, Tanifuji M. Intrinsic signal imaging in macaque retina reveals different types of flash-induced light reflectance changes of different origins. Invest. Opthamol. Visual Sci 2007;48:2903–2912.
21. Hanazono G, Tsunoda K, Kazato Y, Tsubota K, Tanifuji M. Evaluating Neural Activity of Retinal Ganglion Cells by Flash-evoked Intrinsic Signal Imaging in Macaque Retina. Invest. Opthamol. Visual Sci. 2008
22. Inomata K, Tsunoda K, Hanazono G, Kazato Y, Shinoda K, Yuzawa M, Tanifuji M, Miyake Y. Distribution of retinal responses evoked by transscleral electrical stimulation detected by intrinsic signal imaging in macaque monkeys. Invest. Opthamol. Visual Sci 2008;49:2193–2200.
23. Nelson DA, Krupsky S, Pollack A, Aloni E, Belkin M, Vanzetta I, Rosner M, Grinvald A. Special report: Noninvasive multi-parameter functional optical imaging of the eye. Ophthalmic Surg. Lasers Imaging 2005;36:57–66. [PubMed: 15688972]
24. Crittin M, Riva CE. Functional imaging of the human papilla and peripapillary region based on flicker-induced reflectance changes. Neurosci. Lett 2004;360:141–144. [PubMed: 15082153]
25. Abramoff MD, Kwon YH, Ts'o D, Soliz P, Zimmerman B, Pokorny J, Kardon R. Visual stimulus-induced changes in human near-infrared fundus reflectance. Invest. Opthamol. Visual Sci 2006;47:715–721.
26. Yao XC, George JS. Near-infrared imaging of fast intrinsic optical responses in visible light-activated amphibian retina. J. Biomed. Opt 2006;11:064030. [PubMed: 17212553]
27. Yao XC, George JS. Dynamic neuroimaging of retinal light responses using fast intrinsic optical signals. Neuroimage 2006;33:898–906. [PubMed: 17000120]
28. Yao XC, Yamauchi A, Perry B, George JS. Rapid optical coherence tomography and recording functional scattering changes from activated frog retina. Appl. Opt 2005;44:2019–2023. [PubMed: 15835350]
29. Jonnal RS, Rha J, Zhang Y, Cense B, Gao WH, Miller DT. In vivo functional imaging of human cone photoreceptors. Opt. Exp 2007;15:16141–16160.
30. Grieve K, Roorda A. Intrinsic signals from human cone photoreceptors. Invest. Opthamol. Visual Sci 2008;49:713–719.

31. Bizheva K, Pflug R, Hermann B, Povazay B, Sattmann H, Qiu P, Anger E, Reitsamer H, Popov S, Taylor JR, Unterhuber A, Ahnelt P, Drexler W. Optophysiology: depth-resolved probing of retinal physiology with functional ultrahigh-resolution optical coherence tomography. Proc. Natl. Acad. Sci. U S A 2006;103:5066–5071. [PubMed: 16551749]
32. Fercher AF, Hitzenberger CK, Kamp G, Elzaiat SY. Measurement of Intraocular Distances by Backscattering Spectral Interferometry. Opt. Commun 1995;117:43–48.
33. Häusler G, Lindner MW. “Coherence radar” and “spectral radar”-new tools for dermatological diagnosis J. Biomed. Opt 1998;3:21–31.
34. Srinivasan VJ, Wojtkowski M, Fujimoto JG, Duker JS. In vivo measurement of retinal physiology with high-speed ultrahigh-resolution optical coherence tomography. Opt. Lett 2006;31:2308–2310. [PubMed: 16832468]
35. Wojtkowski M, Leitgeb R, Kowalczyk A, Bajraszewski T, Fercher AF. In vivo human retinal imaging by Fourier domain optical coherence tomography. J. Biomed. Opt 2002;7:457–463. [PubMed: 12175297]
36. Leitgeb R, Hitzenberger CK, Fercher AF. Performance of Fourier domain vs. time domain optical coherence tomography. Opt. Exp 2003;11:889–894.
37. Wojtkowski M, Srinivasan VJ, Ko TH, Fujimoto JG, Kowalczyk A, Duker JS. Ultrahigh-resolution, high-speed, Fourier domain optical coherence tomography and methods for dispersion compensation. Opt. Exp 2004;12:2404–2422.
38. Srinivasan VJ, Monson BK, Wojtkowski M, Bilonick RA, Gorczynska I, Chen R, Duker JS, Schuman JS, Fujimoto JG. Characterization of outer retinal morphology with high-speed, ultrahigh-resolution optical coherence tomography. Invest. Opthamol. Visual Sci 2008;49:1571–1579.
39. Anger EM, Unterhuber A, Hermann B, Sattmann H, Schubert C, Morgan JE, Cowey A, Ahnelt PK, Drexler W. Ultrahigh resolution optical coherence tomography of the monkey fovea. Identification of retinal sublayers by correlation with semithin histology sections. Exp. Eye Res 2004;78:1117–1125. [PubMed: 15109918]
40. Gloesmann M, Hermann B, Schubert C, Sattmann H, Ahnelt PK, Drexler W. Histologic correlation of pig retina radial stratification with ultrahigh-resolution optical coherence tomography. Invest. Opthamol. Visual Sci 2003;44:1696–1703.
41. Zhang Y, Cense B, Rha J, Jonnal RS, Gao W, Zawadzki RJ, Werner JS, Jones S, Olivier S, Miller DT. High-speed volumetric imaging of cone photoreceptors with adaptive optics spectral-domain optical coherence tomography. Opt. Exp 2006;14:4380–4394.

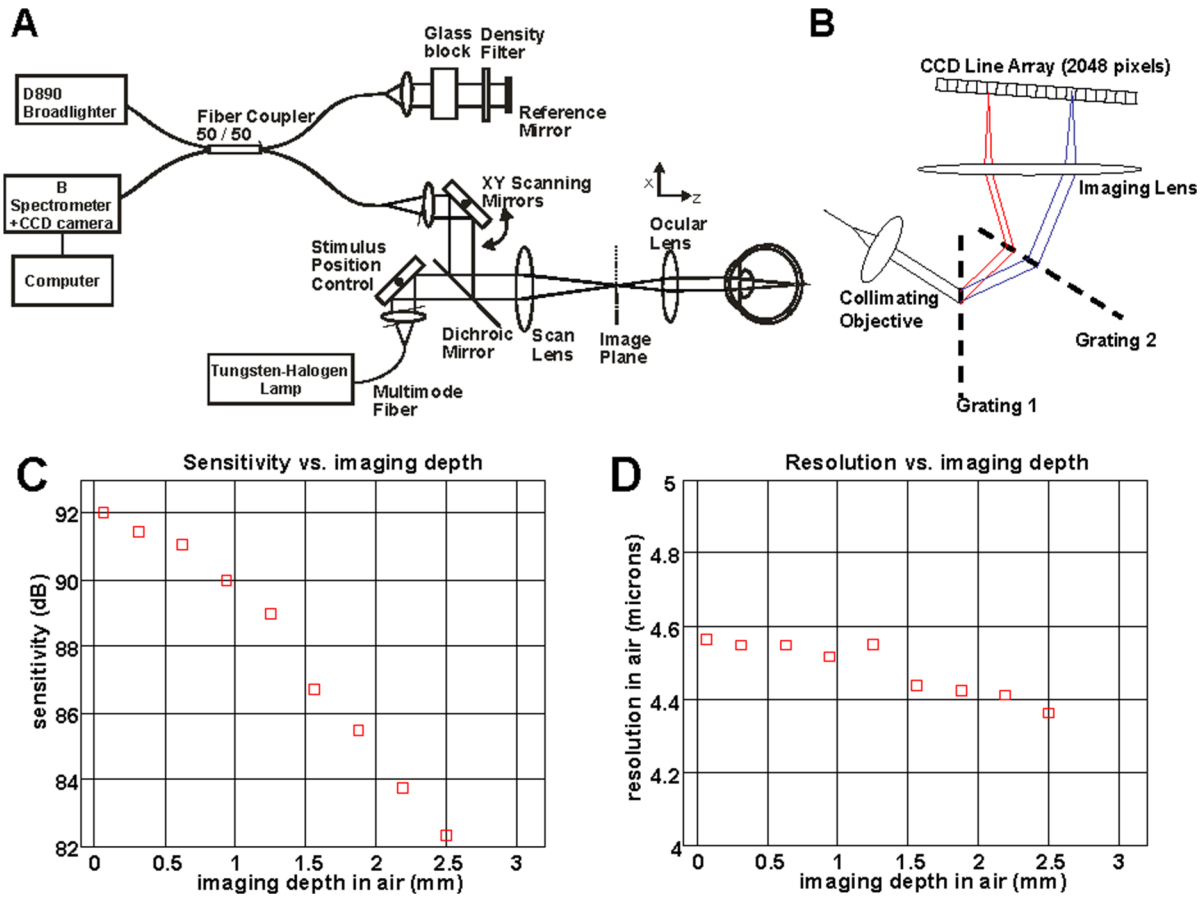

Fig. 1.

Schematic of OCT system (a) and spectrometer (b) used for functional OCT experiments. (c) Measured sensitivity drop as a function of imaging depth in air. (d) Measured resolution in air as a function of imaging depth in air for the spectrometer design shown. The resolution was measured as the full-width at half maximum (FWHM) of the point spread function amplitude in air, without accounting for water absorption in the eye.

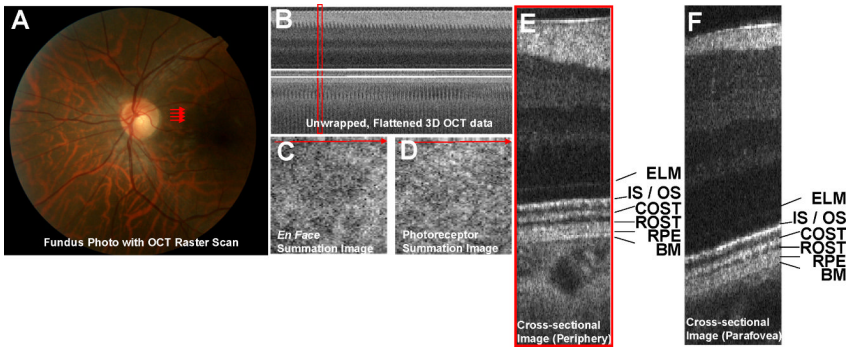

Fig. 2.

(a) Fundus photograph with OCT raster scan shown in red. (b) Unwrapped 3D OCT data set, flattened to the IS / OS junction. Because the data set is flattened to the IS / OS junction, the IS / OS junction appears at the same axial position across the image. (c) *En face* image obtained by summing over the entire retina. (d) *En face* image obtained by summing over the photoreceptors only. The axial range corresponding to the photoreceptors is shown by two horizontal white lines in (b). (e) Cross-sectional image in the periphery showing the outer retina in detail. The location of this cross-sectional image is shown in red in (b)-(d). (F) Cross-sectional image obtained from a raster scan of the parafovea showing the outer retina in detail. The corresponding raster scan is not shown. (ELM – external limiting membrane, IS / OS – photoreceptor inner segment / outer segment junction, COST – cone outer segment tips, ROST – rod outer segment tips, RPE – retinal pigment epithelium, BM – Bruch's membrane)

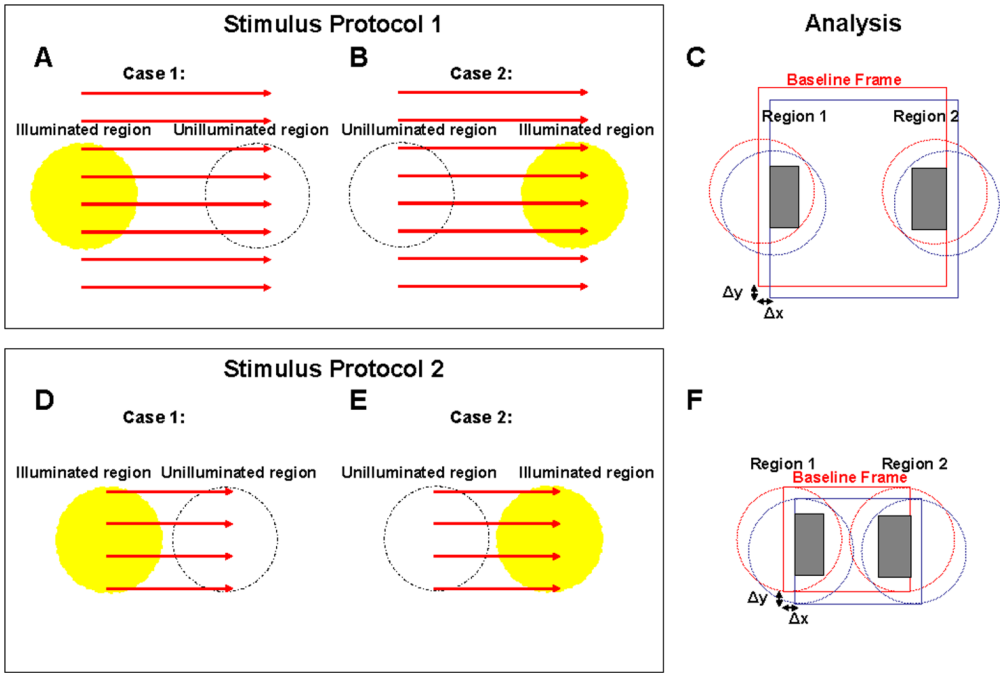

Fig. 3.

(a-b) Stimulus protocol 1 for functional experiments in human subjects. An OCT raster scan of 128 images × 168 axial scans, shown in red, is repeated, generating 2 volumes / second. For each trial, one side of the field is randomly selected for illumination, corresponding to one of the two cases shown in (a-b). (c) Analysis of the functional experiment. The analysis procedure for each region is the same whether or not it was illuminated for a particular trial. For each frame within a trial, correlation is performed to determine portions of region 1 and region 2 that overlap with the baseline frame. Only the areas shaded in gray are used to determine the fractional changes in normalized reflectance described by Eq. (1)-(4). (d-f) Stimulus protocol 2 and analysis used for functional experiments. For this protocol, an OCT raster scan of 64 images × 112 axial scans, shown in red, is repeated, generating 6 volumes / second.

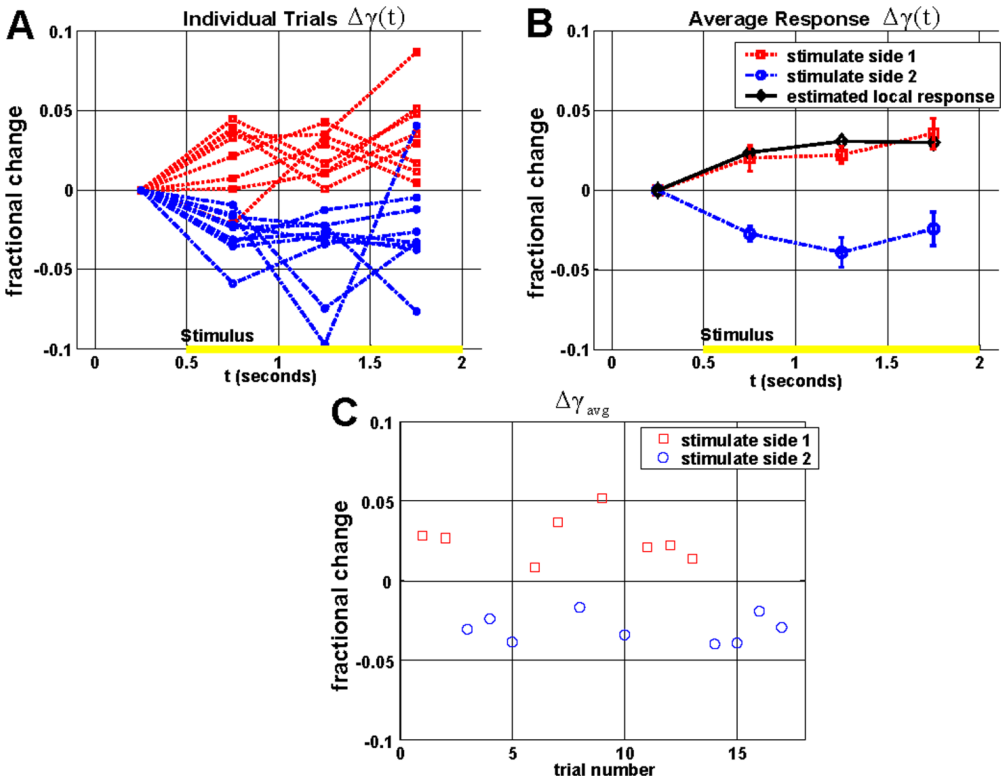

Fig. 4.

Response from the IS / OS junction in the parafovea ($r_{Sig} = r_{ISOS}$, $r_{Ref} = r_{RPE}$). (a) The individual trials show that when region 1 is illuminated, $\Delta\gamma_1(t)$ increases relative to $\Delta\gamma_2(t)$ after the stimulus, and when region 2 is illuminated, $\Delta\gamma_2(t)$ increases relative to $\Delta\gamma_1(t)$ after the stimulus. (b) The average time courses for each group are shown, along with standard errors. The estimated local response is shown in black, and represents an increase in reflectance of the IS / OS junction. (c) A scatter plot of $\Delta\gamma_{avg}$ shows a clear difference between the two groups ($p < 1e\text{-}7$, two-tailed t-test). Results were obtained with protocol 1.

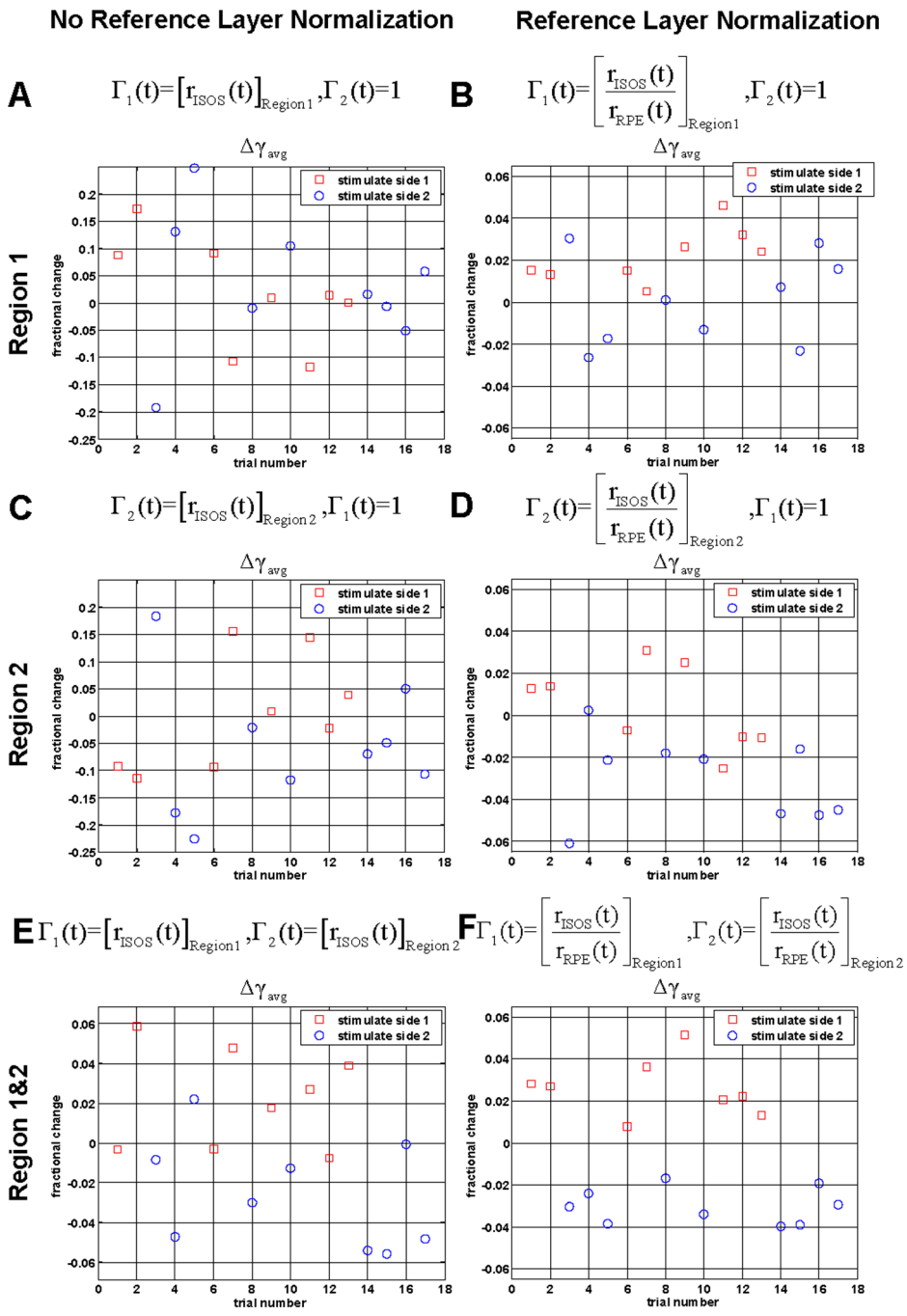

Fig. 5.

(a-f) Scatter plots showing the effect of the data analysis procedure on the measured functional response. As shown, normalizing to a reference (RPE) layer and comparing two regions of the retina improves discrimination between the two groups. Above each panel are modifications to Eq. (1) – Eq. (2). Results were obtained with protocol 1.

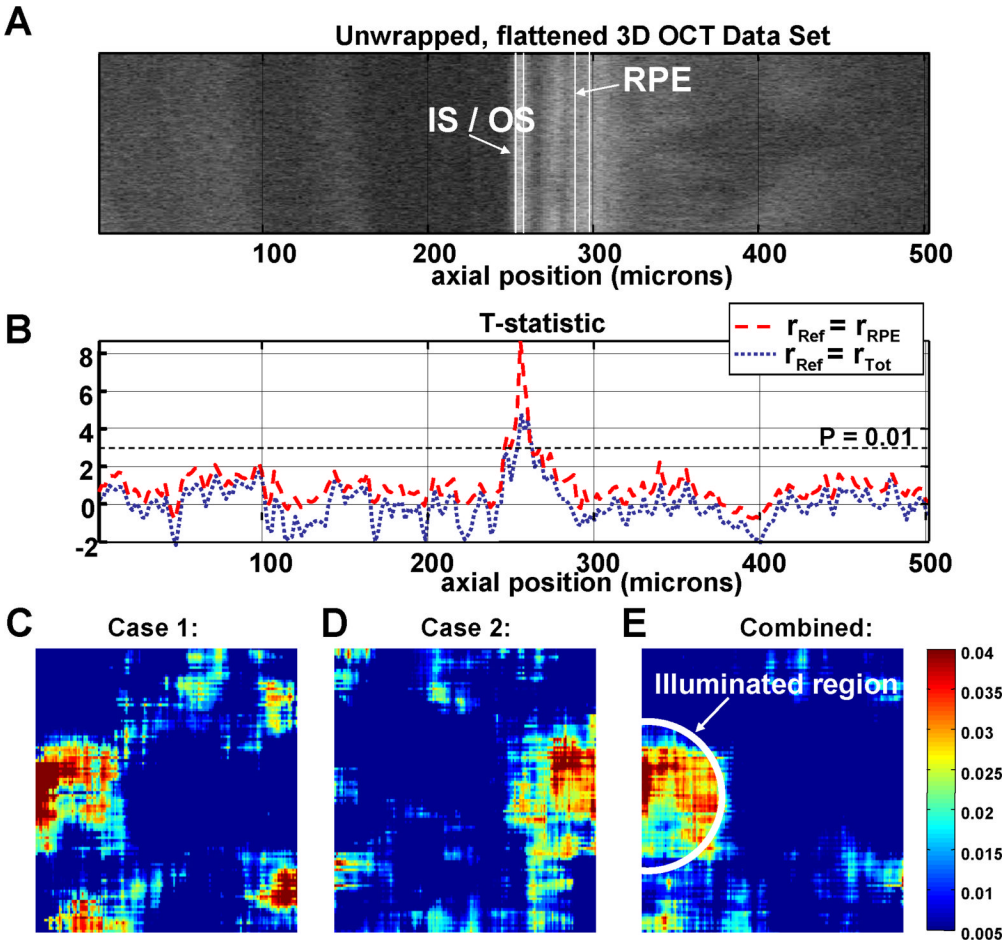

Fig. 6.

(a) An unwrapped 3D OCT data set from the parafovea, illustrating the variation in anatomy over the region scanned for the functional experiment. The data set has been flattened to the IS / OS junction. Axial position (Z) is shown in microns on the horizontal axis. (b) The t-statistic is plotted as a function of axial position using either $r_{Ref} = r_{RPE}$ (red dashed line) or $r_{Ref} = r_{Tot}$ (blue dotted line). As shown, the only axial position with a high t-statistic corresponds to the IS / OS junction. (c-d) Averaged differential photoreceptor response map described in Eq. (9) is shown in colorscale. The average is performed over 8 trials (c) and 9 trials (d) to reduce noise. Median filtering of the map reduces speckle noise and noise from registration errors. (e) Because of good correspondence between the illumination location and the functional response, a combined differential map can by formed by averaging all 17 trials by flipping the differential maps from case 2 (Fig. 3(b)) so that the illuminated regions correspond. Results were obtained with protocol 1.

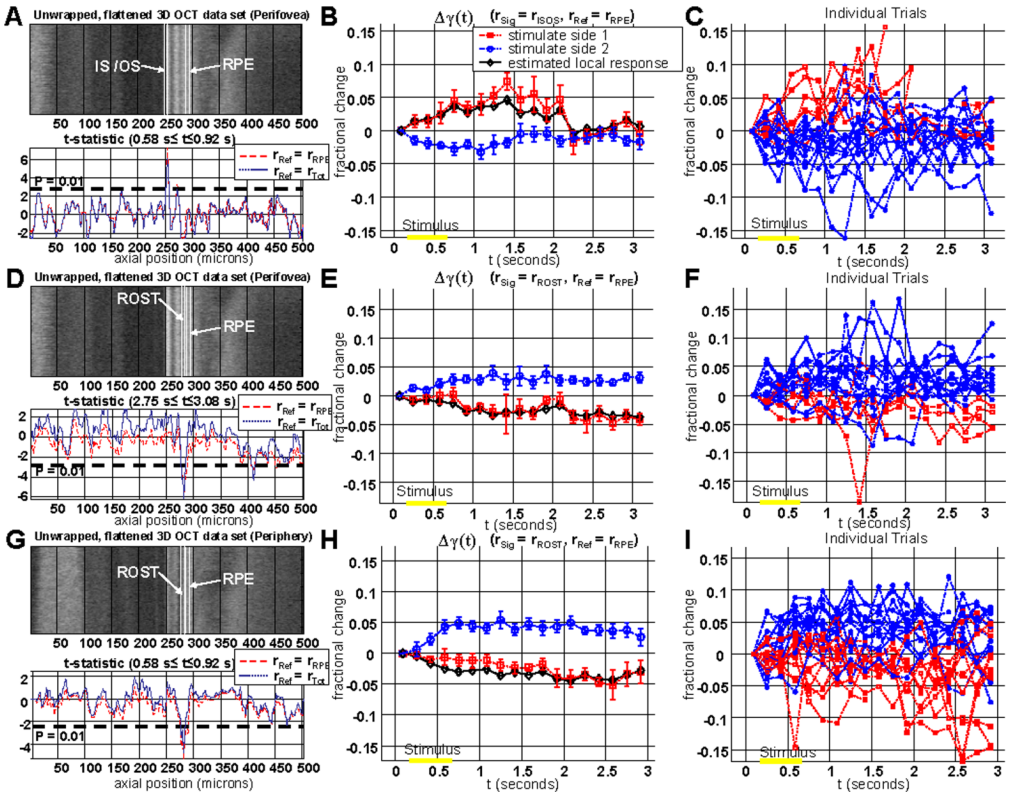

Fig. 7.

Comparison of photoreceptor responses in the perifovea (a-f) and periphery (g-i). (a) In the perifovea, the t-statistic plot (0.58 s ≤ t ≤ 0.92 s) showed a positive peak at the IS / OS junction, as expected based on the previous results. (b-c) The time course of the IS / OS reflectance change shows a return to baseline by t=2.5 s. (d) In the perifovea the t-statistic plot (2.75 s ≤ t ≤ 3.08 s) showed a negative peak at the rod outer segment tips (ROST). The plot in D did not show a positive peak at the IS / OS junction as seen in A because the t-statistic was computed at a later time interval. A later time interval is chosen to compute the t-statistic for the ROST response because the reflectance change in the ROST layer is delayed (e-f). In the periphery, there was no response seen at the IS / OS junction (g). However, a negative response is clearly seen at the position corresponding to the ROST (g-i). The ROST layer is only a few microns anterior to the RPE. Results were obtained with protocol 2.